Nano Energy 60 (2019) 630–640

Contents lists available at ScienceDirect

Nano Energy

journal homepage: www.elsevier.com/locate/nanoen

Full paper

3D mathematical model of contact-separation and single-electrode mode triboelectric nanogenerators

Jiajia Shao[a,b], Morten Willatzen[a,b,*], Yijun Shi[c], Zhong Lin Wang[a,b,d]

[a] CAS Center for Excellence in Nanoscience, Beijing Key Laboratory of Micro-nano Energy and Sensor, Beijing Institute of Nanoenergy and Nanosystems, Chinese Academy of Sciences, Beijing, 100083, China
[b] College of Nanoscience and Technology, University of Chinese Academy of Sciences, Beijing, 100049, People's Republic of China
[c] Division of Machine Elements, Department of Engineering Sciences and Mathematics, Luleå Tekniska Universitet, Luleå, Sweden
[d] School of Materials Science and Engineering, Georgia Institute of Technology, Atlanta, GA, 30332-0245, United States

ARTICLE INFO

Keywords:
triboelectric nanogenerator
3D mathematical model
Displacement current
Contact-mode
Single-electrode mode

ABSTRACT

Based on a set of finite-sized charged planes (FSCP), a simple time-dependent three-dimensional spatial model for the electric potential and electric field in an inhomogeneous medium composed of dielectric materials and metal contacts is proposed and used to assert triboelectric nanogenerator operation. Solving the problem of FSCP makes the three-dimensional spatial model relevant for practical TENG applications and allow for accurate and reliable results. Connecting the metal contacts to an electric resistance, Kirchhoff's law is used to derive a first-order time-dependent differential equation for the mobile charges on the metal contacts and the displacement current. Specially, the displacement current (Maxwell's displacement current) in a TENG equals to the conduction current in the external circuit is obtained. We then consider two important types of triboelectric nanogenerators: the contact-separation (CS) mode and the single-electrode (SEC) mode. A forced movement of the dielectric materials and/or the metal contacts leads to currents flowing in the system and a time-varying electrical potential, and therefore the generation of electrical power. Then, new and more accurate capacitance equations for CS and SEC modes of TENGs are extracted. Several examples of energy harvesting scenarios are finally analyzed.

1. Introduction

Triboelectric nanogenerators (TENGs) have received extensive attention due to numerous applications in the area of energy harvesting and self-powered sensors, demonstrating their promising potential to power the next generation of mobile and randomly distributed electronic devices [1–8]. Although triboelectric effects are usually undesirable, for TENGs they provide a useful and applicable strategy to harvest energy from low-frequency environmental vibrations and motions [9,10].

In order to develop an efficient design of TENG structures and a more accurate prediction of their output characteristics, an in-depth understanding of triboelectric material selection, static triboelectric charge (density), and time-varying electric fields is a prerequisite. Hence, accurate simulation models that fit practical realizations of TENGs are urgently necessary. In fact, selection of triboelectric materials mostly depends on semi-empirical triboelectric series (SETS), built according to the electron donor-receptor behavior of various materials [11,12]. In the SETS, different materials are arranged within a column where materials close to the top tend to lose electrons when in contact or rubbing the materials below them [13]. Once the triboelectric materials of TENGs are selected, an external force generates tribo-electric charges at the contacting surfaces because of the different work functions of the materials, or due to ion transfer, charged material transfer and so on [14–16]. Owing to leakage through the dielectric or surrounding gas, triboelectric decharging may result, but the triboelectric charge can be replenished by virtue of a series of contact-separation steps that eventually lead to a steady state saturated triboelectric charge value [17,18]. Furthermore, these triboelectric charges will create an electric field not only between the two contacting surfaces (or air-gap) but also in the dielectric materials [19]. Also, due to the presence of triboelectric charges, image charges will be induced in the metal electrodes resulting in a new modulated electric field distribution [20]. Recent years have witnessed many phenomena that can be attributed to

* Corresponding author. CAS Center for Excellence in Nanoscience, Beijing Key Laboratory of Micro-nano Energy and Sensor, Beijing Institute of Nanoenergy and Nanosystems, Chinese Academy of Sciences, Beijing, 100083, China
E-mail address: morwi@fotonik.dtu.dk (M. Willatzen).

https://doi.org/10.1016/j.nanoen.2019.03.072
Received 22 December 2018; Received in revised form 4 March 2019; Accepted 21 March 2019
Available online 24 March 2019
2211-2855/

a spatiotemporal varying electric field such as edge effects and the gas (air) breakdown [10,21,22]. In addition, as the air-gap distance changes with time, the induced charge densities increase/decrease and lead to a time-dependent electric field, meanwhile the displacement current between the two metal electrodes of TENGs [23,24]. From an electrodynamics point of view, the time-varying electric field is the physical effect responsible for TENG operation. However, although the electric field plays an important role for the output behavior of TENGs, studying the effect has not been much of a priority till now [17,25]. One reason is that a detailed and reliable model which can explain the working mechanism of TENGs has not been available [9,10,18,19].

In this paper, we present a time-dependent and universal three-dimensional (3D) spatial model for TENGs based on Maxwell's equations. We derive a system of equations for the time-varying electrical potential, electric field, mobile charges, current, and electrical power from a set of finite-sized charged planes (FSCP). Solving the problem of FSCP makes the three-dimensional spatial model relevant for practical TENG applications and allow for accurate and reliable results. More importantly, we show how the time-varying electric field influences the operation of TENGs. From the time-varying electric field we determine the associated displacement current and conclude that the displacement current generated in a TENG equals to the conduction current in the external circuit. Two typical models, the contact-separation and single-electrode modes of TENGs are considered and our theoretical results show excellent agreement with a previously published model (DDEF model) [19]. Next, we derive capacitance equations based on the 3D spatial model for the CS and SEC modes of TENGs. Furthermore, a comprehensive analysis of energy harvesting scenarios for various electrical loadings, triboelectric charges, and mechanical excitations is discussed in detail providing a direct visualization of advantages and disadvantages of the different operating conditions.

2. General theory

We first derive a general expression for the electric potential due to a number of finite-sized charged planes. We will consider the medium as being composed of different dielectric materials containing triboelectric charges. The composed medium is sandwiched between two electrodes with free charges [16,19]. The Maxwell-Poisson equation

$$\nabla\cdot\mathbf{D} = \rho(\mathbf{r}) \tag{1}$$

where ρ is the charge density of free movable charges (on the electrodes) and triboelectric charges in the dielectric media. We shall assume the constitutive relation

$$\mathbf{D}(\mathbf{r}) = \varepsilon(\mathbf{r})\mathbf{E}(\mathbf{r}) \tag{2}$$

holds locally everywhere in the dielectric material. Since the dynamics is considered weak (low frequency variations), magnetic field effects can be neglected. We then have $\nabla\times\mathbf{E}=0$ and the electric field is fully specified by a scalar potential

$$\mathbf{E} = -\nabla\phi \tag{3}$$

Thus, we have in the dielectric material α with constant permittivity ε_α:

$$-\nabla\cdot(\varepsilon(\mathbf{r})\nabla\phi) = -\varepsilon_\alpha\nabla^2\phi = \rho(\mathbf{r}) \tag{4}$$

where $\mathbf{r}$ is the position in the dielectric material α where the electric potential is to be evaluated. An integral solution for φ in the dielectric material α is

$$\phi(\mathbf{r}) = \frac{1}{4\pi\varepsilon_\alpha}\int\frac{\rho(\mathbf{r}')}{|\mathrm{r}-\mathrm{r}'|}dV \tag{5}$$

3. Electric potential from a set of charged finite-sized planes

Assume we have N finite-sized planes, all with the same geometric dimensions a and b along the x and y directions, respectively. The planes are all centered at $(x, y) = (0, 0)$ and located at positions $z_1, \ldots, z_N$ with surface charges $\sigma_1, \ldots, \sigma_N$, respectively. From Eq. (5), the electric potential at an *arbitrary* point $\mathbf{r} = (x, y, z)$ is

$$\begin{aligned}\phi(x,y,z) &= \sum_{i=1}^{N}\int_{-a/2}^{a/2}\int_{-b/2}^{b/2}\frac{\sigma_i dx'dy'}{4\pi\varepsilon(\mathbf{r})\sqrt{(x-x')^2+(y-y')^2+(z-z_i)^2}}\\ &= \sum_{i=1}^{N}\frac{\sigma_i}{4\pi\varepsilon(\mathbf{r})}\int_{-a/2}^{a/2}\int_{-b/2}^{b/2}\frac{dx'dy'}{\sqrt{(x-x')^2+(y-y')^2+(z-z_i)^2}}\end{aligned} \tag{6}$$

Where $\varepsilon_\alpha = \varepsilon(\mathbf{r})$, and the electric field is

$$\begin{aligned}\mathbf{E}(x,y,z) &= -\nabla\phi\\ &= \sum_{i=1}^{N}\frac{\sigma_i}{4\pi\varepsilon(\mathbf{r})}\int_{-a/2}^{a/2}\int_{-b/2}^{b/2}\frac{dx'dy'}{(x-x')^2+(y-y')^2+(z-z_i)^2}\\ &\quad\frac{(x-x',\,y-y',\,z-z_i)}{\sqrt{(x-x')^2+(y-y')^2+(z-z_i)^2}}\end{aligned} \tag{7}$$

Evaluating the electric field as a function of the z coordinate at the center of the planes, where $x = y = 0$, we find that E_x and E_y vanish identically due to antisymmetry when integrating over the x' and y' directions. The electric field component along the z direction is

$$E_Z(0,0,z) = \sum_{i=1}^{N}\frac{\sigma_i(z-z_i)}{4\pi\varepsilon(\mathbf{r})}\int_{-a/2}^{a/2}\int_{-b/2}^{b/2}\frac{dx'dy'}{(x'^2+y'^2+(z-z_i)^2)^{3/2}} \tag{8}$$

The latter integral can be evaluated analytically:

$$\begin{aligned}&\int_{-a/2}^{a/2}\int_{-b/2}^{b/2}\frac{dx'dy'}{(x'^2+y'^2+(z-z_i)^2)^{3/2}}\\ &= \frac{4}{z-z_i}\arctan\left(\frac{ab}{4(z-z_i)\sqrt{\left(\frac{a}{2}\right)^2+\left(\frac{b}{2}\right)^2+(z-z_i)^2}}\right)\end{aligned} \tag{9}$$

3.1. Plate capacitor

Let us revisit the classical nearly infinite-sized plate capacitor problem. In this case, we have a charge q distributed on the plate located at $z = z_L$ corresponding to a surface charge $\sigma = q/(ab)$. At $z = z_R$ there is a charge $-q$ corresponding to a surface charge $\sigma = -q/(ab)$. From the latter two equations we find equal contributions from the two plates to the electric field between the plates, and the electric field becomes

$$\begin{aligned}E_Z(0,0,z) &= \frac{\sigma(z-z_L)}{4\pi\varepsilon_\alpha}\frac{4}{z-z_L}\lim_{a,b\to\infty}\left[\arctan\left(\frac{ab}{4(z-z_L)\sqrt{\left(\frac{a}{2}\right)^2+\left(\frac{b}{2}\right)^2+(z-z_L)^2}}\right)\right]\\ &\quad-\frac{\sigma(z-z_R)}{4\pi\varepsilon_\alpha}\frac{4}{z-z_R}\lim_{a,b\to\infty}\left[\arctan\left(\frac{ab}{4(z-z_R)\sqrt{\left(\frac{a}{2}\right)^2+\left(\frac{b}{2}\right)^2+(z-z_R)^2}}\right)\right]\\ &= \frac{\sigma}{\varepsilon_\alpha}\end{aligned} \tag{10}$$

since

$$\begin{aligned}\lim_{a,b\to\infty}\left[\arctan\left(\frac{ab}{4(z-z_L)\sqrt{\left(\frac{a}{2}\right)^2+\left(\frac{b}{2}\right)^2+(z-z_L)^2}}\right)\right] &= \frac{\pi}{2}\\ \lim_{a,b\to\infty}\left[\arctan\left(\frac{ab}{4(z-z_R)\sqrt{\left(\frac{a}{2}\right)^2+\left(\frac{b}{2}\right)^2+(z-z_R)^2}}\right)\right] &= -\frac{\pi}{2}\end{aligned} \tag{11}$$

when $z_L < z < z_R$. The result in Eq. (10) agrees with the standard

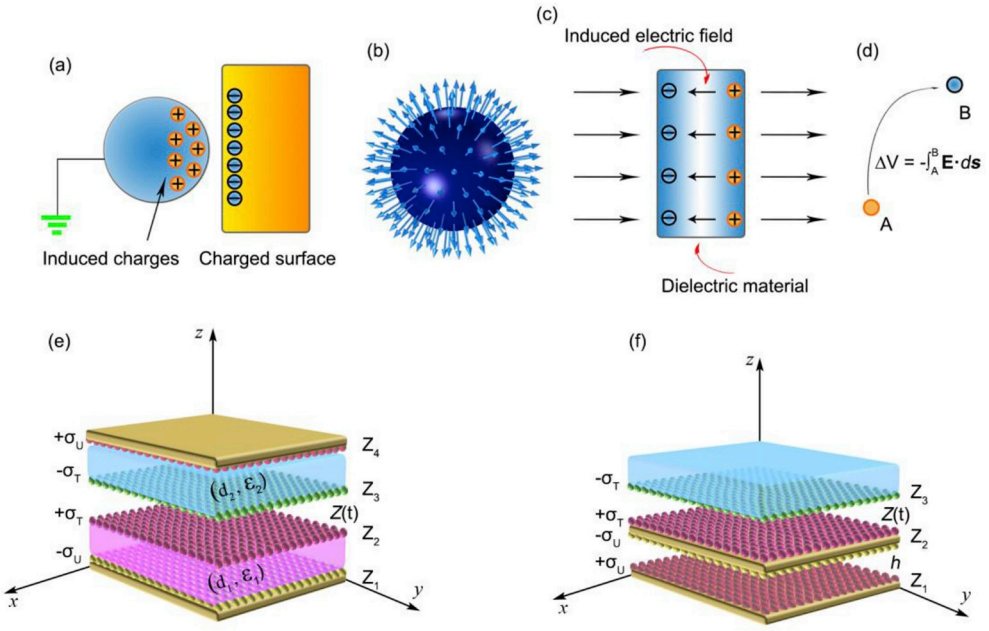

Fig. 1. (a) The charged surface on the right induces charges on the surface of a metallic sphere, and charge is conserved during the induction process. (b) For a positive point charge, its electric field lines are directed radially outward. (c) Electric field is induced in a dielectric material, the amplitude of which is less than the external field. (d) The electric potential difference between A and B in an electric field can be calculated by an integral. Note that the integral does not depend on the path taken from A to B. (e) and (f) Schematic of a typical contact-separation (CS) mode triboelectric nanogenarator (TENG) and a single-electrode (SEC) mode TENG in the rectangular coordinate system, respectively.

result (as it must!) by use of the Maxwell-Poisson equation $\nabla \cdot \mathbf{D} = \rho$ and Gauss's law:

$$\int_V \nabla \cdot \mathbf{D} dV = \int_S \mathbf{D} \cdot \mathbf{n} dA = AD = q \tag{12}$$

Since $\mathbf{D} = \varepsilon_\alpha E$ and $\rho = q/A$.

3.2. The electric potential and Kirchhoff's law

We will now obtain a convenient alternative expression for the electric potential. To this purpose, we will use Leibniz integral rule:

$$\frac{d}{dz}\left(\int_{u(z)}^{v(z)} f(z')dz'\right) = f(v(z))\frac{dv(z)}{dz} - f(u(z))\frac{du(z)}{dz} \tag{13}$$

To write the potential, in the case with charges $-\sigma_u$, σ_T, $-\sigma_T$, σ_u placed at positions z_1, z_2, z_3, z_4, respectively, in an inhomogeneous media consisting of three materials: A dielectric layer with permittivity E_1 containing the triboelectric charge $+\sigma_T$, air with no charges, and a dielectric layer with permittivity E_2 containing the triboelectric charge $-\sigma_T$ (Fig. 1e). In this case the electric potential at $z = z_4$ and $z = z_1$ are given by

$$\begin{aligned}\phi(0,0,z_4) &= -\frac{\sigma_u}{\pi\varepsilon_2}\int_{z_4-z_1}^{\infty} f(z')dz' + \frac{\sigma_u}{\pi\varepsilon_2}\int_0^{\infty} f(z')dz' \\ &+ \frac{\sigma_T}{\pi\varepsilon_2}\int_{z_4-z_2}^{\infty} f(z')dz' - \frac{\sigma_T}{\pi\varepsilon_2}\int_{z_4-z_3}^{\infty} f(z')dz' \\ \phi(0,0,z_1) &= -\frac{\sigma_u}{\pi\varepsilon_1}\int_0^{\infty} f(z')dz' + \frac{\sigma_u}{\pi\varepsilon_1}\int_{z_1-z_4}^{\infty} f(z')dz' \\ &+ \frac{\sigma_T}{\pi\varepsilon_1}\int_{z_1-z_2}^{\infty} f(z')dz' - \frac{\sigma_T}{\pi\varepsilon_1}\int_{z_1-z_3}^{\infty} f(z')dz'\end{aligned} \tag{14}$$

where

$$f(z) = \arctan\left(\frac{ab}{4z\sqrt{\left(\frac{a}{2}\right)^2 + \left(\frac{b}{2}\right)^2 + z^2}}\right) \tag{15}$$

Assume an electrical resistance R is connected to the electrodes. Then the potential over R is

$$\Delta V = RI = -R\frac{dQ}{dt} = -RA\frac{d\sigma_u}{dt} \tag{16}$$

where A is the electrode area, Q is the capacitor charge, and Kirchhoffs' law states

$$-RA\frac{d\sigma_u}{dt} = \phi(0,0,z_4) - \phi(0,0,z_1) \tag{17}$$

Combining Eqs. (14) and (17) determines a time-dependent differential equation in σ_u from which $\sigma_u(t)$ can be fully specified. For completeness, we write the differential equation out:

$$\begin{aligned}-RA\frac{d\sigma_u}{dt} &= \frac{\sigma_u}{\pi\varepsilon_2}\int_0^{z_4-z_1} f(z')dz' + \frac{\sigma_T}{\pi\varepsilon_2}\int_{z_4-z_2}^{z_4-z_3} f(z')dz' \\ &+ \frac{\sigma_T}{\pi\varepsilon_1}\int_{z_1-z_3}^{z_1-z_2} f(z')dz' + \frac{\sigma_u}{\pi\varepsilon_1}\int_0^{z_1-z_4} f(z')dz'\end{aligned} \tag{18}$$

We find, in the absence of triboelectric charges, $\sigma_T = 0$, and for nearly infinite electrode plane areas, that Eq. (18) simplifies to

$$\begin{aligned}-RA\frac{d\sigma_u}{dt} &= \frac{\sigma_u}{\varepsilon_\alpha}(z_4 - z_1) \\ -R\frac{dQ}{dt} &= RI = Ed\end{aligned} \tag{19}$$

which is the well-known Kirchhoff's voltage law for a standard capacitor in series with a resistance R. In obtaining the last equation, we made use of the limiting expressions in Eq. (11) and wrote I, $E = \sigma_u/\varepsilon_\alpha$, and $d = z_4 - z_1$, for the current, the (constant in space) electric field between the capacitor electrodes, and the capacitor thickness, respectively.

3.2.1. Open-circuit conditions

For open-circuit (OC) conditions, the electrode charge densities $\pm\sigma_u$ vanish and the OC voltage becomes

$$\begin{aligned}-V_{OC} = \phi(0,0,z_4) - \phi(0,0,z_1) &= \frac{\sigma_T}{\pi\varepsilon_2}\int_{z_4-z_2}^{z_4-z_3} f(z')dz' \\ &+ \frac{\sigma_T}{\pi\varepsilon_1}\int_{z_1-z_3}^{z_1-z_2} f(z')dz'\end{aligned} \tag{20}$$

3.2.2. Short-circuit conditions

The short-circuit (SC) current is given by

$$I_{SC} = A\frac{d\sigma_u^{SC}}{dt} \tag{21}$$

where A is the electrode area and σ_u^{SC} is the SC electrode charge

density. The latter is found from Eq. (18) by setting the electrical resistance R equal to zero (zero voltage):

$$\sigma_u^{SC} = \frac{\sigma_T\left[\frac{1}{\varepsilon_2}\int_{z_4-z_2}^{z_4-z_3} f(z')dz' + \frac{1}{\varepsilon_1}\int_{z_1-z_2}^{z_1-z_3} f(z')dz'\right]}{\frac{1}{\varepsilon_1}\int_0^{z_1-z_4} f(z')dz' + \frac{1}{\varepsilon_2}\int_0^{z_4-z_1} f(z')dz'} \tag{22}$$

Note that $\sigma_u^{SC}(t)$ is determined immediately by the (constant-in-time) triboelectric charge σ_T and integrals with integration limits involving the time-dependent values of z_1, z_2, z_3, z_4.

3.2.3. Energy output

The instantaneous power is given by

$$P(t) = \Delta V(t) I(t) = RI(t)^2 = R\left(A\frac{d\sigma_u}{dt}\right)^2 \tag{23}$$

and the integrated output energy E reads

$$E = \int_0^t P(t')dt' \tag{24}$$

3.2.4. Forced motion and initial conditions

In the numerical examples we present in the following two types of forced motion and initial conditions are considered.

Forced motion and initial condition 1: Oscillatory motion is enforced by assuming

$$x(t) = \frac{x_{\max}}{2}\left(1 - \cos\left(\frac{\pi v t}{x_{\max}}\right)\right) \tag{25}$$

and the electrode charge density satisfies initially

$$\sigma_u(t=0) = 0 \tag{26}$$

Forced motion and initial condition 2: The charge density satisfies $\sigma_u(t = x_{\max}/v) = \sigma_0$, where σ_0 is the charge density obtained from Eq. (18) assuming the forced oscillatory motion defined by Eq. (25) and the initial condition $\sigma_u(t=0) = 0$. At any time $t \geq x_{\max}/v$, the electrode carrier density $\sigma_u(t)$ is then obtained from Eq. (18) assuming the air gap $x(t)$ is fixed at $x_{\max}$. Hence, the electrode charge density experiences a relaxation in time (for $t \geq x_{\max}/v$) due to the presence of the load resistance R.

4. Numerical experiments

In Fig. 2, we plot the electrical potential as a function of the thickness of the air gap, i.e., $|z_3 - z_2|$, for OC conditions of the TENG shown in Fig. 1e. An oscillatory variation in the air-gap thickness is enforced (Fig. 2a) (***Forced movement and initial condition 1***). The calculated potentials $\varphi_a = \varphi(0, 0, z_1)$ and $\varphi_b = \varphi(0, 0, z_4)$ and the OC voltage $V_{OC} = \varphi_a - \varphi_b$ are shown in Fig. 2b. As one would expect, the peak values of φ_a, φ_b increase sharply with the increase of the air-gap thickness and begin to saturate at an air-gap thickness above approximately 0.2 m (Fig. 2c). In Fig. 2d, the temporal values of V_{OC} are plotted using the present model [Finite-Sized Charged Planes (FSCP)] vs. results of the Distance-Dependent Electric Field (DDEF) model of Dharmasena et al. [19] and the capacitance (CA) model [10and26]. In Fig. 2e, the peak value of the OC voltage is plotted vs. the maximum air-gap thickness for the three models. Evidently, the present model and the DDEF model are in exact agreement while the simpler CA model leads to rather different qualitative and quantitative results. The OC voltage values as a function of time are considerably larger for the CA model compared to the FCSP and DDEF models.

In **Fig. 3a**, we plot the charge density σ_u vs. time according to Eq. (22) subject to an oscillatory variation of the air-gap thickness of the form given by Fig. 2a (***Forced movement and initial condition 1***) and for SC conditions. We then compute in Fig. 3b the maximum value of σ_u as a function of time vs. the maximum value of the air-gap thickness. It is clear again that the FSCP and DDEF model agree while deviations are found for the CA model. Fig. 3c shows a plot of the total charge vs. time for the three computational schemes with the same conclusions. In Fig. 3d, the SC current I_{SC} is plotted vs. time using Eq. (21). As before, the peak values are somewhat smaller using the CA model scheme compared to the FSCP and DDEF schemes. It follows from Fig. 3e that the peak current increases with increasing frequency of the forced air-gap thickness oscillatory motion for all air-gap thicknesses. This result is due to I_{SC} being proportional to the time derivative of the charge density (Eq. (21)). In Fig. 3f, results for the SC current are plotted using the three models FCSP, DDEF, and CA. It is clear that the maximum SC current is a linear function of the frequency. Furthermore, the air gap $x(t)$ vs. time at SC conditions is depicted in Fig. S1a. Comparison of σ_u and I_{SC} at different frequencies using the FSCP and CA models are shown in Fig. S1, plots b and c.

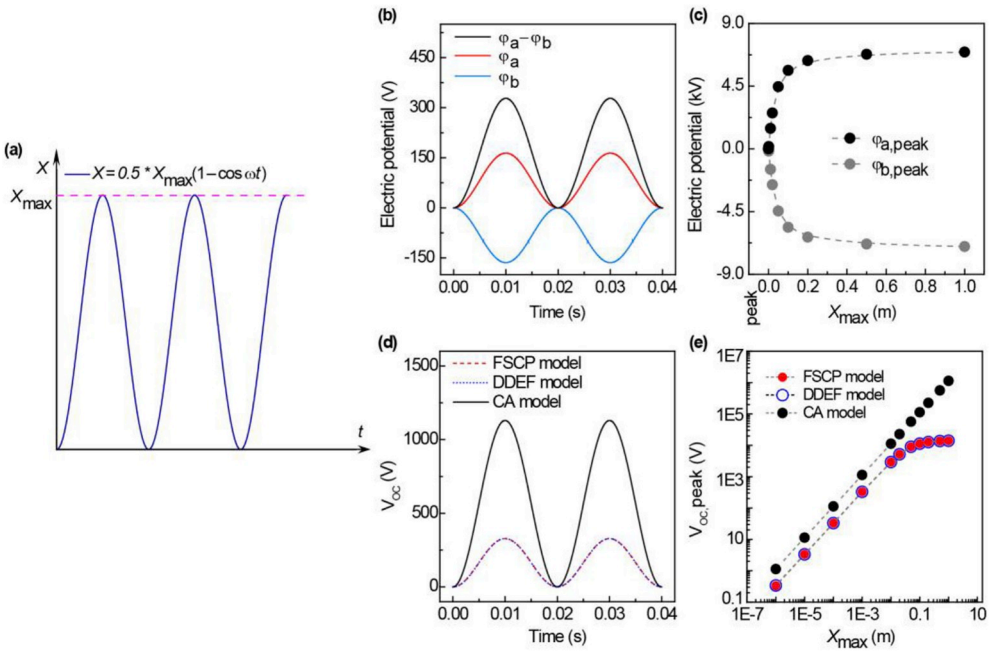

Fig. 2. (a) Electric potential variations for a forced oscillatory distance of the air-gap thickness subject to open-circuit (OC) conditions. (b) The electric potential and potential difference vs. time for different maximum contact-separation distance ($x_{\max}$) at OC conditions. (c) Peak electric potential for different $x_{\max}$ at OC conditions. (d) Comparison of the potential difference at OC conditions (V_{OC}) from the FSCP model, DDEF model and CA model [10,26]. (e) Comparison of the peak V_{OC} for different $x_{\max}$ from the three different models.

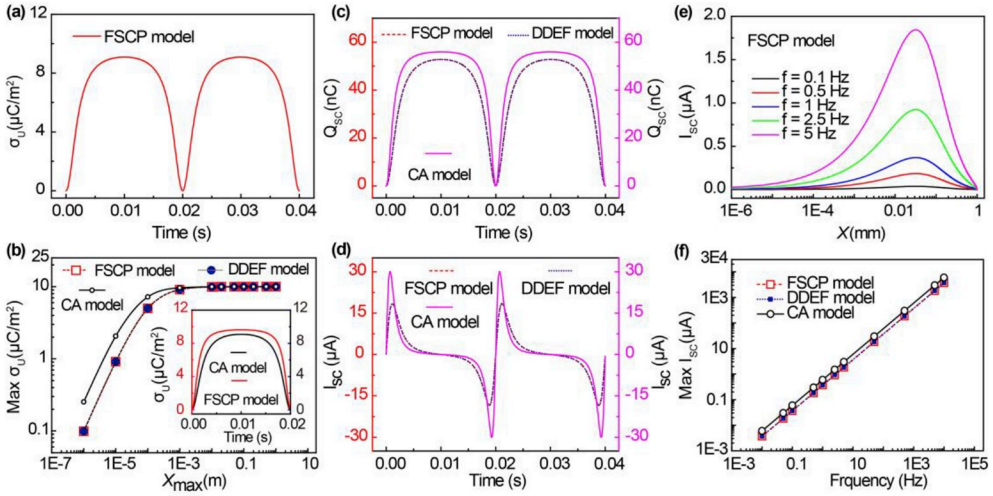

Fig. 3. Charge and current variations for a forced oscillatory distance of the air-gap thickness subject to SC conditions. (a) The transferred charge density (σ_u) from the FSCP model at short-circuit (SC) conditions. (b) Comparison of the maximum σ_u from the three different models at different x_{max}. The inset shows a comparison of σ_u vs. time at SC conditions for the two models: FSCP model and CA model. (c) Comparison of the transferred charges (Q_{SC}) and (d) short-circuit current (I_{SC}) from the three different models at SC conditions.(e) Comparison of the short-circuit current (I_{SC}) at different frequencies using the FSCP model. (f) Comparison of the peak I_{SC} at different frequencies from the three different models.

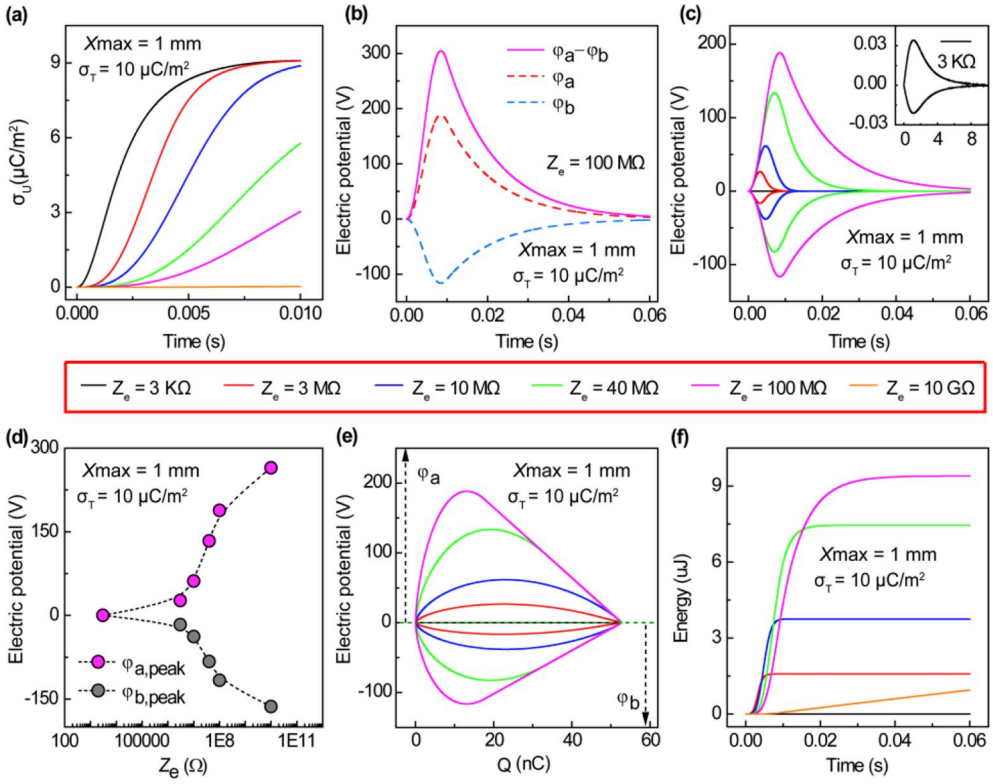

Fig. 4. Output characteristics for a forced time dependence of the air-gap thickness subject to different triboelectric charge densities using the present FSCP model. (a) Charge density σ_u vs. time for different load conditions. (b) The electric potential and potential difference vs. time with load resistance R = 100 MΩ. (c) The electric potential and potential difference vs. time for different load resistances. (d) The peak electric potential for different load resistances. (e) The encircled areas of the electric potential-transferred charges curves for different load resistances, equivalent to the harvested energy in a half cycle movement. (f) Harvested energy vs. time for different load conditions.

In Fig. 4, we plot output characteristics in the case of an electrical resistance R coupled to the electrodes subject to ***Forced movement and initial condition 2***. Results for the electrode charge density as a function of time are shown in Fig. 4a for electrical resistances in the range 3 kΩ–10 kΩ assuming a triboelectric charge density σ_T equal to 10μC/m^2. As expected the charge density decreases with increasing electrical resistance at any time and, eventually, approaches zero as the resistance becomes high enough (near-OC conditions). In Fig. 4b the potentials at the electrodes first increase and reach their peak values at around 0.01 s before they all drop to nearly zero at a time of 0.06s. In Fig. 4c, the electric potential ΔV is shown as a function of time for different electrical resistances. Evidently, the voltage across the electrodes increases with the electrical resistance. Values are given up to an electrical resistance of 100 MΩ. The peak electrode voltage values are shown in Fig. 4d for electrical resistance values up to 10 GΩ. A voltage saturation begins to set in for electrical resistances above 10 GΩ. In Fig. 4e and f the voltage-total charge and harvested energy are shown corresponding to different electrical resistance (loading) conditions. Note that the energy, plotted in Fig. 4f is the area between the respective curves and the x axis in Fig. 4e. The harvested energy increases with an increasing electrical load as expected. Especially, the electric potential, potential difference, and transferred total charges vs. time for various electrical resistances are depicted in Fig. S2. The peak electric potentials at the two electrodes are mainly determined by the flow of transferred charges. The electric field changes strongly in accordance herewith. Firstly, the peak electric potential occurs at the position where the electric field changes most drastically as can be seen in **Fig. 6**, plots d-e, where Z_1 and Z_3 represent the positions of the top dielectric-electrode

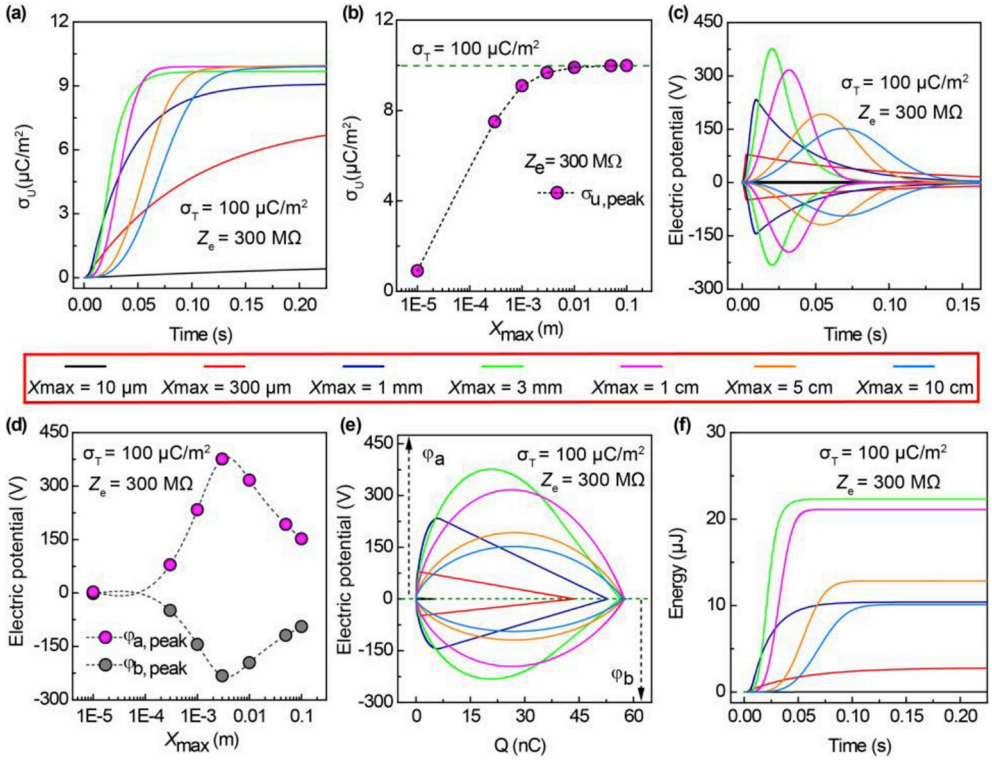

Fig. 5. Output characteristics for a forced time dependence of the air-gap thickness subject to different air-gap thickness amplitudes using the present FSCP model (a) Charge density σ_u vs. time for different x_{max}. (b) Peak σ_u for different x_{max} with load resistance R = 300 MΩ. (c) The electric potential and potential difference vs. time for different x_{max}. (d) Peak electric potential for different x_{max}. (e) The encircled areas of the electric potential-transferred charges curves for different x_{max}, equivalent to the harvested energy in a half cycle movement. (f) Harvested energy vs. time for different x_{max}.

interface and bottom dielectric-electrode interface, respectively. Secondly, the total electric field response at the dielectric-electrode interface depends on the electrical resistance, and result in different magnitudes and locations of the peak electrical potential.

In addition, at moderate load resistance values a maximum peak power generation is obtained. This load resistance is denoted the optimum resistance. For instance, in Fig. S9a the optimum power is about 1 mW and occurs at an optimum resistance of 100 MΩ. This corresponds to a situation where the load resistance is the same as the internal TENG resistance. Further details on optimum power generation and load resistance vs. TENG internal resistance can be found in, e.g., Refs. [9,10,19].

Further, more, Fig. S3 shows the dependence of the electrode charge and the electric potential across the electrodes vs. time and the triboelectric charge for a fixed electrical resistance of 3 MΩ and assuming ***Forced movement and initial condition 2***. In Fig. S3a the time dependence of the triboelectric charge is plotted as a function of time corresponding to an air-gap thickness of 1 mm for a series of triboelectric charge values in the range 1–150 μC/m^2. The peak electrode charge vs. the triboelectric charge is shown in Fig. S3b. Evidently, there is a clear linear relationship. Fig. S3c shows the potential across the electrodes as a function of time for different triboelectric charge density values. Fig. 5d is a plot of the peak potential vs. the triboelectric charge density. Fig. S3, plots e-f show the potential vs. the total charge and the energy output, respectively. It's clear that the higher the triboelectric charge density the higher the energy output for a certain air-gap thickness amplitude. The air gap $x(t)$ and potential difference $\Delta\varphi$ vs. time for different surface charge densities σ_T are depicted in Fig. S4, plots a and b, respectively. Fig. S4, plots c-d show the peak $\Delta\varphi$ and harvested energy for different σ_T values. Evidently, a higher σ_T value leads to a higher σ_u and faster changes in the electric field (Fig. 6, plots g-h), and therefore a higher electric potential and potential difference. Hence, a higher σ_T value significantly improves the output performance/power generation of the TENG.

Plots along the same lines as in Fig. 4, S3 are shown in **Fig. 5** for a variation of the amplitude of the air-gap thickness at a fixed electrical resistance equal to 300 MΩ (**Forced movement and initial condition 2**). It's interesting to note that a maximum voltage across the electrodes is obtained for an air-gap amplitude of about 3 mm. The voltage drops for higher air-gap thickness amplitudes since the air-gap thickness change occurs at constant v value, equal to 0.1 m/s, for all x_{max} values. This behavior is also reflected in the energy output. The air gap $x(t)$ and potential difference $\Delta\varphi$ vs. time for different x_{max} values are depicted in Fig. S5, plots a and b, respectively. Fig. S5, plots c and d show the peak Δφ and harvested energy for different x_{max} values. It is found that the maximum $\Delta\varphi$ and harvested energy are obtained when x_{max} = 3 mm. The reason is that at this air gap thickness, the internal resistance of the TENG is close to the electrical resistance (300MΩ). A systematic discussion has been given in Refs. [9,10,19]. The optimum choice of R, x_{max}, and σ_T depend intimately on the external loading conditions. Hence, the best choices of R, x_{max}, and σ_T for power generation must be obtained by optimizing the total TENG resistance to the external load.

5. Displacement current through a finite-sized capacitor

Science $\mathbf{D} = \varepsilon(\mathbf{r})\mathbf{E}$ and the displacement current I_D through a surface S is defined by

$$I_D = \int_S \frac{\partial \boldsymbol{D}}{\partial t} \cdot \mathbf{n} dS \tag{27}$$

where $\mathbf{n}$ is a normal vector to the surface element dS, we have from Eq. (7) that the displacement current along the z direction (perpendicular to the capacitor plates) is

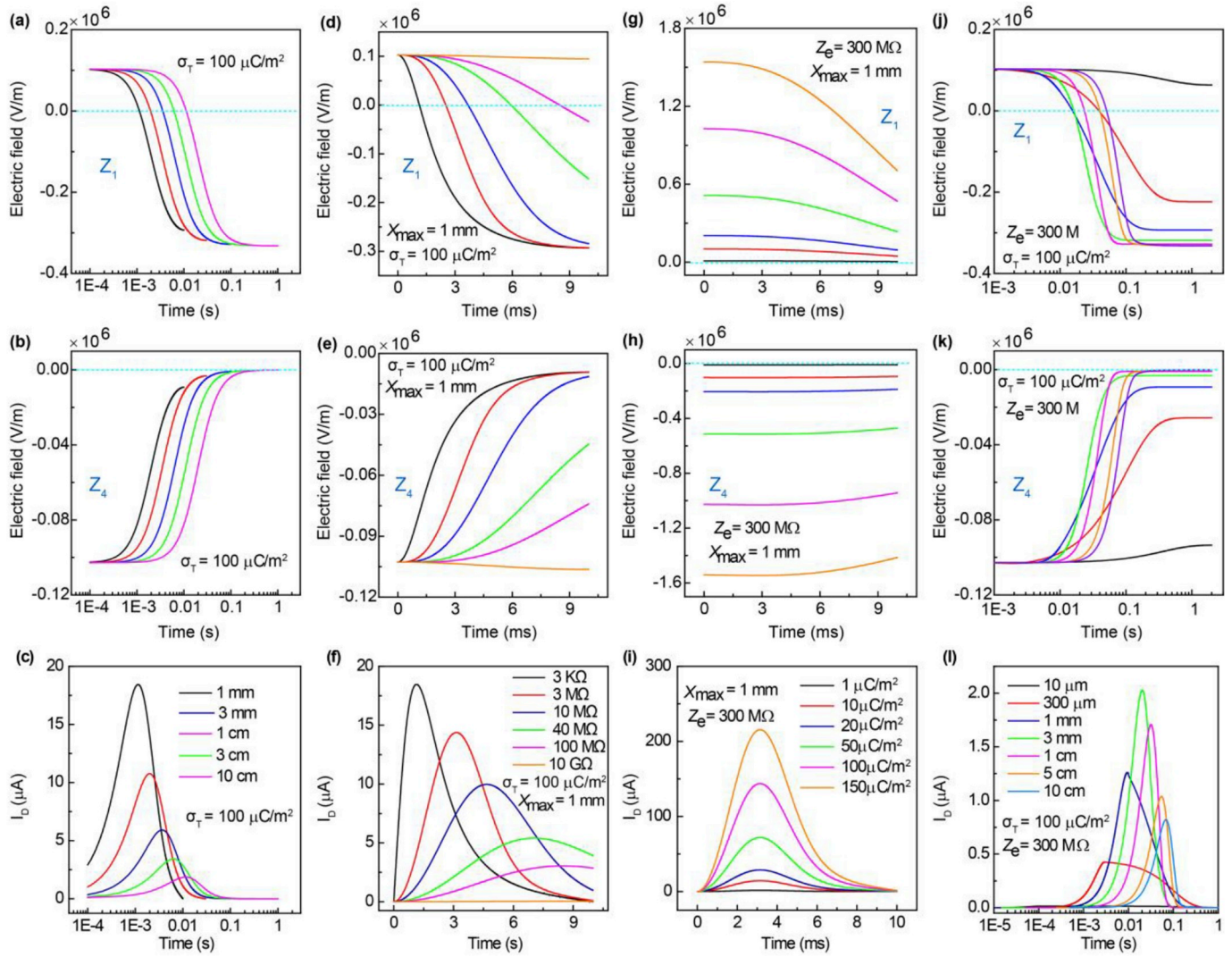

Fig. 6. Electric field and current characteristics for a forced time dependence of the air-gap thickness using the present FSCP model. The electric field vs. time at the positions (a) z_1, (b) z_4, and (c) the corresponding I_D at SC conditions. The electric field vs. time at the positions (d, g, j) z_2, (e, h, k) z_4, and (f, i, l) the corresponding I_D for different R, σ_T, and x_{max}, respectively.

$$I_D = \sum_{i=1}^{N} \int_S dS \frac{\partial}{\partial t}\left(\frac{\sigma_i}{4\pi}\int_{-a/2}^{a/2}\int_{-b/2}^{b/2} dx'dy' \frac{z-z_i}{((x-x')^2+(y-y')^2+(z-z_i)^2)^{3/2}}\right) \tag{28}$$

If S extends over the full $x-y$ plane, including the region outside the area defined by the capacitor plates, it is easy to show that I_D is constant in z and given by

$$\begin{aligned} I_D &= \sum_{i=1}^{N}\int_{-\infty}^{\infty} dx \int_{-\infty}^{\infty} dy \frac{\partial}{\partial t}\left(\frac{\sigma_i}{4\pi}\int_{-a/2}^{a/2}\int_{-b/2}^{b/2} dx'dy' \frac{z-z_i}{((x-x')^2+(y-y')^2+(z-z_i)^2)^{3/2}}\right) \\ &= \sum_{i=1}^{N} \frac{\partial}{\partial t}\left(\frac{\sigma_i}{4\pi}\int_{-a/2}^{a/2}\int_{-b/2}^{b/2} dx'dy' \frac{z-z_i}{((x-x')^2+(y-y')^2+(z-z_i)^2)^{3/2}}\right) \\ &= ab\sum_{i=1}^{N}\int_{-\infty}^{\infty} dx_1 \int_{-\infty}^{\infty} dy_1 \frac{\partial}{\partial t}\left(\frac{\sigma_i}{4\pi}\frac{z-z_i}{(x_1^2+y_1^2+(z-z_i)^2)^{3/2}}\right) \end{aligned} \tag{29}$$

where, in obtaining the third equality, we have used that the integrand is not a function of x' and y' due to the substitution of variables x, y by $x_1 = x - x'$, $y_1 = y - x'$. In the typical capacitor case, we have opposite charge densities, σ and $-\sigma$, on the two plates. Then, use of Eq. (9) yields

$$I_D = ab\frac{\partial \sigma}{\partial t} = \frac{\partial q}{\partial t} \tag{30}$$

where $q = ab\sigma$ is the total charge on one capacitor plate. Note that this is the standard result for the displacement current through a capacitor. We conclude that this simple expression is still fulfilled in the case of a finite-size capacitor despite the fact that the electric field is not confined to the region between the capacitor plates due to edge effects. It is apparent that the above derivation is applicable to the different modes of TENGs. For the TENG, we have

$$I_D = I = \frac{\partial q}{\partial t} \tag{31}$$

Hence, the displacement current generated in a TENG equals the conduction current I in the external circuit. Note that the derivation above can be easily extended to the general case with several charged planes ($N > 2$).

5.1. Electric field for CS mode operation

For CS mode operation, the electric field from the four charged planes can be written as

$$E_Z(0,0,z) = -\frac{\sigma_u}{\pi\varepsilon(z)}\arctan\left(\frac{ab}{4(z-z_1)\sqrt{\left(\frac{a}{2}\right)^2+\left(\frac{b}{2}\right)^2+(z-z_1)^2}}\right) + \frac{\sigma_T}{\pi\varepsilon(z)}\arctan\left(\frac{ab}{4(z-z_2)\sqrt{\left(\frac{a}{2}\right)^2+\left(\frac{b}{2}\right)^2+(z-z_2)^2}}\right) - \frac{\sigma_T}{\pi\varepsilon(z)}\arctan\left(\frac{ab}{4(z-z_3)\sqrt{\left(\frac{a}{2}\right)^2+\left(\frac{b}{2}\right)^2+(z-z_3)^2}}\right) + \frac{\sigma_u}{\pi\varepsilon(z)}\arctan\left(\frac{ab}{4(z-z_4)\sqrt{\left(\frac{a}{2}\right)^2+\left(\frac{b}{2}\right)^2+(z-z_4)^2}}\right) \quad (32)$$

where $\varepsilon(z)$ is the permittivity at position z. Hence, $\varepsilon(z)$ is a step function depending only on which of the three material layers we evaluate the electric field in. The electric field inside the air gap (between the z_3 and z_2), dielectric 1 and dielectric 2 are defined as $E_{z,\mathrm{air}}(0, 0, Z_{\mathrm{air}})$, $E_{z,\mathrm{d1}}(0, 0, Z_{\mathrm{d1}})$ and $E_{z,\mathrm{d2}}(0, 0, Z_{\mathrm{d2}})$, respectively; and the related capacitances are C_{air}, C_{d1}, and C_{d2}, respectively. Based on the electric field equation of (32), we can evaluate these electric fields and capacitances, the capacitance equations for the CS model TENG (C_{CS}) with edge effects is (**Supplementary Note** 2b):

$$C_{\mathrm{CS}} = \frac{\pi\varepsilon_0\varepsilon_1\varepsilon_2 ab}{F(0,0,z_{\mathrm{d1}})d_1\varepsilon_2 + F(0,0,z_{\mathrm{air}})z(t)\varepsilon_1\varepsilon_2 + F(0,0,z_{\mathrm{d2}})d_2\varepsilon_1} \quad (33)$$

where

$$F(0,0,Z_{\mathrm{air}}) = f(Z_{\mathrm{air}} - Z_2) - f(Z_{\mathrm{air}} - Z_3),$$

$$F(0,0,Z_{\mathrm{d1}}) = f(Z_{\mathrm{d1}} - Z_1) - f(Z_{\mathrm{d1}} - Z_2) + f(Z_{\mathrm{d1}} - Z_3) - f(Z_{\mathrm{d1}} - Z_4),$$

$F(0, 0, Z_{\mathrm{d2}}) = f(Z_{\mathrm{d2}} - Z_1) - f(Z_{\mathrm{d2}} - Z_2) + f(Z_{\mathrm{d2}} - Z_3) - f(Z_{\mathrm{d2}} - Z_4)$; and $d_1 < Z_{\mathrm{air}} < d_1 + z(t)$, $0 < Z_{\mathrm{d1}} < d_1$, $d_1 + x_{\max} < Z_{\mathrm{d2}} < d_1 + x_{\max} + d_2$. Comparison of numerical results of C_{CS} calculated using Eq. (33) vs. results for the CA model when considering the influence of one edge is depicted in Fig. S6. In addition, if there is only one dielectric included (for instance, dielectric 2) in the CS mode TENG, the related C_{CS} can also be derived (**Supplementary Note** 2b).

In Fig. 6, we plot the electric field vs. time for different $x_{\max}$ values at positions $z = z_1$ and $z = z_3$ in Fig. 6a, d, g, j and Fig. 6b, e, h, k, respectively (***Forced movement and initial condition 2***). The electric field vs. time relationships are plotted for different R, σ_T, and air gap maximum values in Fig. 6d, g, j for $z = z_1$ and (e,h,k) for $z = z_3$. The displacement current I_D for the same set of different R, σ_T, and air gap maximum values are shown in Fig. 6f, i, l. At SC conditions, the electric field vs. time at the positions z_2 and z_3 for different R, σ_T, and $x_{\max}$ is shown in Fig. S8. The positions z_2 and z_3 are the locations where the static charges $\pm\ \sigma_T$ are distributed.

It is clear that the total electric field response at the dielectric-electrode interface (z_1) is positive when z(t) increases and the initial position is at $z = 0$. Then, a positive electrical potential is generated at the bottom electrode (Figs. 4c, 5c and 6c). In addition, a negative electric potential is generated at the top electrode. When the two electrodes are connected, the non-zero resistance R reduces the rate of the transferred charge compared to SC conditions. Thus, different profiles of the electric fields (Fig. 6, plots a and d) result. As the air-gap thickness increases, the electric field first becomes 0 and then negative at z_1. The electric field at z_2 and z_3 are always positive and negative, respectively (Fig. S8). Note also that the electric field at z_1 and z_4 is proportional to the surface charge density σ_T.

The displacement current between the electrodes, through any surface perpendicular to the z direction, can be computed using Eqs. 27 and 28. Results are shown in Fig. 6, plots c, f, i, and l. We note that the displacement current is equivalent to the conduction current through the external circuit as Eq. (30) reveals.

6. Single-electrode mode operation

Consider the structure in Fig. 1f used in single-electrode mode operation (SEC) of a TENG. The electric field component evaluated at the center ($x = 0$, $y = 0$) of the charged planes and perpendicular to the charged planes (along the z direction) can be written as

$$E_Z(0,0,z) = \frac{\sigma_u}{\pi\varepsilon_0}f(z-z_1) - \frac{\sigma_u}{\pi\varepsilon_0}f(z-z_2) + \frac{\sigma_T}{\pi\varepsilon_0}f(z-z_2) - \frac{\sigma_T}{\pi\varepsilon_0}f(z-z_3) \quad (34)$$

when evaluated in the air region between the charged planes and assuming the electrode thicknesses are negligibly small compared to the air-gap thicknesses. Then the related actual capacitances between z_3 and z_2 (C_{a}), z_3 and z_1 (C_{b}), and z_2 and z_1 (C_{SEC}) can be obtained (**Supplementary Note** 2c). For example, C_{SEC} is:

$$C_{SEC} = \frac{\pi\varepsilon_0 ab}{F(0,0,z_{SEC})h} \quad (35)$$

where $F(0, 0, Z_{\mathrm{SEC}}) = f(Z_{\mathrm{SEC}} - Z_1) - f(Z_{\mathrm{SEC}} - Z_3)$, and $0 < Z_{\mathrm{SEC}} < h$. Comparison of numerical results of C_{SEC} are plotted in Fig. S7 using Eq. (35) vs. results of the CA model when considering the influence of one edge. The electric potential reads

$$\phi(0,0,z_1) = \frac{\sigma_u}{\pi\varepsilon_0}\int_0^\infty f(z')dz' - \frac{\sigma_u}{\pi\varepsilon_0}\int_{z_1-z_2}^\infty f(z')dz' + \frac{\sigma_T}{\pi\varepsilon_0}\int_{z_1-z_2}^\infty f(z')dz' - \frac{\sigma_T}{\pi\varepsilon_0}\int_{z_1-z_3}^\infty f(z')dz'$$

$$\phi(0,0,z_2) = \frac{\sigma_u}{\pi\varepsilon_0}\int_{z_2-z_1}^\infty f(z')dz' - \frac{\sigma_u}{\pi\varepsilon_0}\int_0^\infty f(z')dz' + \frac{\sigma_T}{\pi\varepsilon_0}\int_0^\infty f(z')dz' - \frac{\sigma_T}{\pi\varepsilon_0}\int_{z_2-z_3}^\infty f(z')dz' \quad (36)$$

Hence, the electrical potential across the electrodes is

$$\Delta\phi = \phi(0,0,z_2) - \phi(0,0,z_1) = \frac{\sigma_u}{\pi\varepsilon_0}\int_{z_2-z_1}^0 f(z')dz' - \frac{\sigma_u}{\pi\varepsilon_0}\int_0^{z_1-z_2} f(z')dz' + \frac{\sigma_T}{\pi\varepsilon_0}\int_0^{z_2-z_3} f(z')dz' - \frac{\sigma_T}{\pi\varepsilon_0}\int_{z_1-z_2}^{z_1-z_3} f(z')dz' \quad (37)$$

and Kirchhoff's law implies

$$\Delta\phi = -RA\frac{d\sigma_u}{dt} \quad (38)$$

In Figs. 6 and 7, we show single-electrode mode results of the electric potential at positions $z = z_1$ and $z = z_2$ denoted φ_a and φ_b, respectively, and their difference subject to ***Forced motion and initial condition 2***. The electric potentials and their difference are computed using Eqs. 36 and 37. In Fig. 7a, the electric potentials and potential difference-time relationship with load resistance $R = 100\,\mathrm{G\Omega}$ are shown. Fig. 7, plots b, d and g show the electric potential vs. time for different (b) R, (d) σ_T and (g) $x_{\max}$. Note that the upper (lower) curves in Fig. 7b and d with the same color correspond to φ_a (φ_b). (c, e and h) The encircled areas of the electric potential-transferred charge curves with different (c) R, (e) σ_T, and (h) $x_{\max}$ are equivalent to the harvested energy in a half cycle movement. Fig. 7, plots f and i show the peak electric potential with different (f) σ_T and (i) $x_{\max}$. The electric potential, potential difference, and harvested energy (Fig. 7, plots d, f and Fig. S12, S13) are all proportional to the triboelectric surface charge density σ_T. In particular, when the distance h between the electrodes is

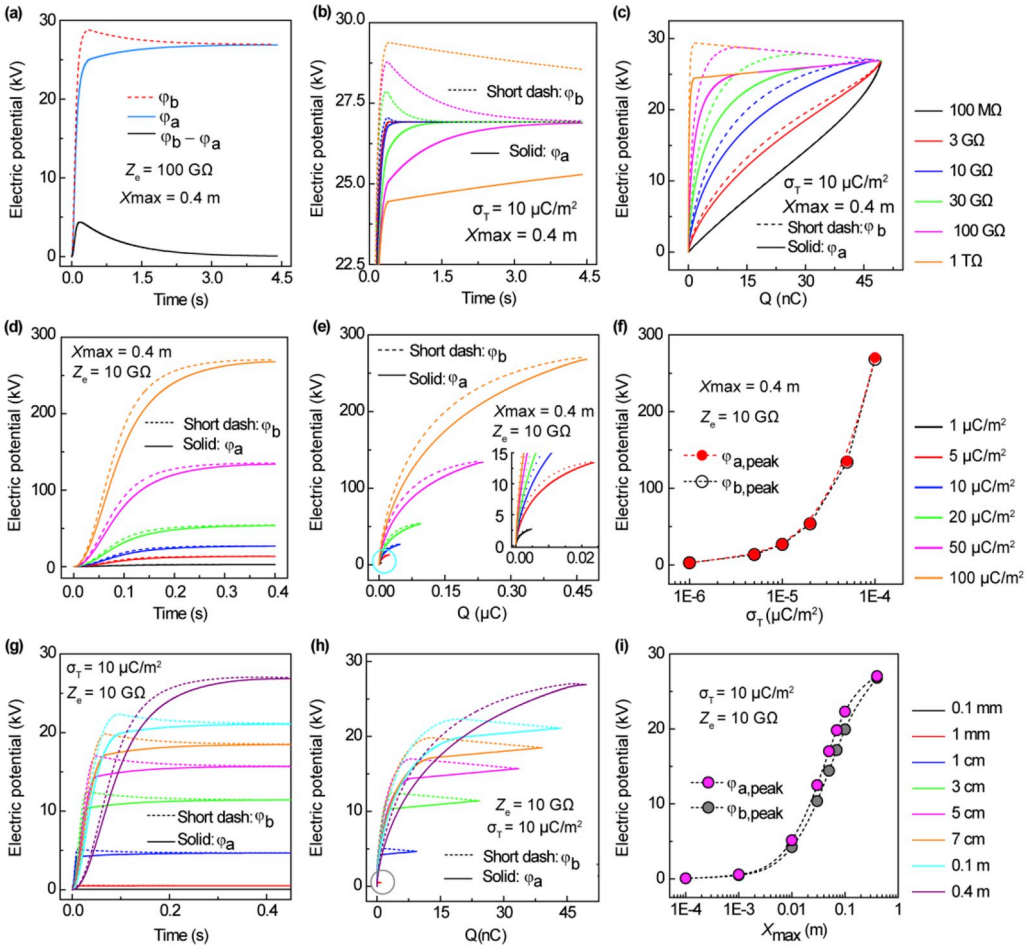

Fig. 7. Electric potential and potential difference of the SEC mode. (a) The electric potential and potential difference vs. time with load resistance $R = 100$ GΩ. (b) The electric potential vs. time for different load resistances. (c) The encircled areas of the electric potential-transferred charges curves for different load resistances, equivalent to the harvested energy in a half cycle movement. (d) Electric potential vs. time for different σ_T values. (e) The encircled areas of the electric potential-transferred charges curves for different σ_T values, equivalent to the harvested energy in a half cycle movement. (f) Peak electric potential for different σ_T values. (g) Electric potential vs. time for different x_{max}. (h) The encircled areas of the electric potential-transferred charges curves for different x_{max}, equivalent to the harvested energy in a half cycle movement. (i) Peak electric potential for different x_{max}.

fixed (0.01 m in the present case), the output of the TENG strongly depends on the air-gap thickness (Fig. 7, plots g, h, i and Fig. S14, S15) in agreement with earlier observations [9,18].

In **Fig. 8**, the electric field and the displacement current are shown for ***Forced motion and initial condition 2*** in the case of single-electrode mode operation. Results are computed using Eqs. (30) and (34). We also plot the electric field-time relationships at the positions of (subplots a, d, g) $z = z_1$ and (subplots b, e, h) $z = z_3$, and the corresponding I_D vs. time (subplots c, f, i) for different R, σ_T, and x_{max}, respectively. In Fig. 8, plots a, d, and g, the SEC mode TENG electric field behavior is seen to be qualitatively different from the CS mode TENG. This is due to a smaller distance (h) between the electrodes for the SEC mode. When h is small (here 0.01 m), the electric field contribution from charges at z_3 strongly affects the electrode charging. As h increases, this electric field contribution decreases and, eventually, the total electric field at z_1 becomes positive (Fig. S18). On the other hand, the electric field at z_3 changes little as the resistance R assumes a large range of values (Fig. 8b). At a sufficiently large $z(t)$, the transferred charge density σ_u saturates at half the value of the triboelectric charge density σ_T (Fig. S11b, S15e). Further, the electric field contributions from charges at z_1 and z_2 are negligibly small compared to the electric field contribution from charges at z_3 (Fig. S16). The displacement current I_D of the SEC mode TENG is smaller than that of the CS mode TENG because of the reduced charge transfer between the electrodes for the former mode.

7. Conclusions

Using Kirchhoff's law, we have derived a time-dependent and general three-dimensional spatial model for the electric potential and electric field in the presence of a distribution of static triboelectric charges in an inhomogeneous medium composed of dielectric materials and metals. The nanogenerators considered are of the contact-separation and single-electrode mode types. A system of equations for the time-varying electrical potential, electric field, mobile charges, and current are derived for two typical modes of TENGs from a set of finite-sized charged planes. A forced displacement of the nanogenerator materials leads to dynamic charges on the metal contacts, currents flowing and a time-dependent voltage across the metal contacts and, hence, the generation of electrical power. In particular, from the time-varying electric field, we determine the generated displacement current in a TENG and conclude that the displacement current is equal to the conduction current in the external circuit, which is important for understanding the nature of TENGs. The capacitance equations based on the 3D spatial model for the CS and SEC modes of TENGs are also derived, and we conclude that the numerical calculations are very similar to these results calculated using the CA model when considering edge effects. Finally, we analyze different mechanical excitations, electrical loadings, and triboelectric charge cases for the harvesting of electrical power and assert advantages and disadvantages of the various operating scenarios.

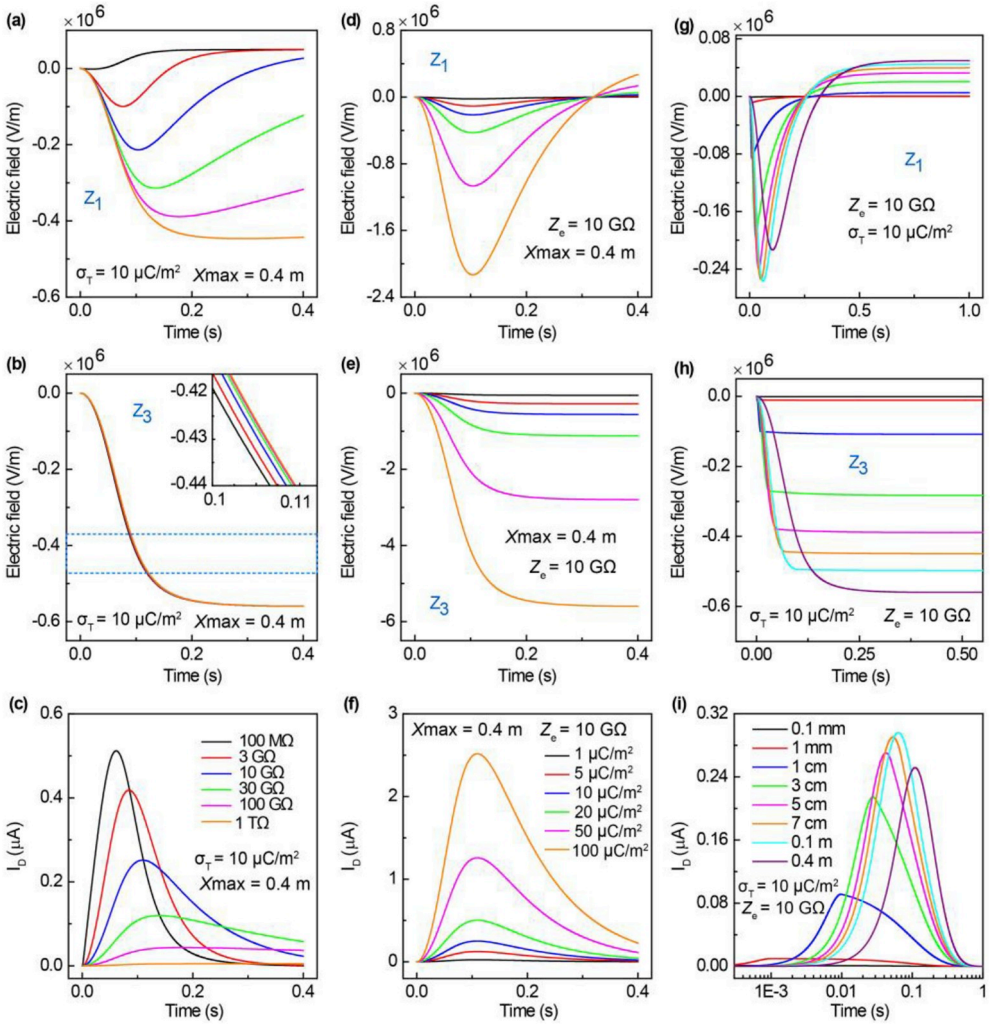

Fig. 8. Electric field and displacement currents for the SEC mode. Electric field and current characteristics for a forced time dependence of the air-gap thickness using the present FSCP model. The electric field vs. time at the positions (a, d, g) z_1, (b, e, h) z_3, and (c, f, i) the corresponding I_D for different R, σ_T, and x_{max}, respectively.

Acknowledgements

Research was sponsored by the National Key R & D Project from Minister of Science and Technology (2016YFA0202704), the National Science Foundation (DMR-1505319) (materials synthesis and application in sensors), Beijing Municipal Science & Technology Commission (Z171100000317001, Z171100002017017, Y3993113DF), National Natural Science Foundation of China (Grant No. 51432005, 5151101243, 51561145021).

Appendix B. Supplementary data

Supplementary data related to this article can be found at https://doi.org/10.1016/j.nanoen.2019.03.072.

References

[1] F.R. Fan, Z.Q. Tian, Z.L. Wang, Flexible triboelectric generator, Nano Energy 1 (2012) 328–334.
[2] W.F. Harper, Contact and Frictional Electrication, Clarendon Press, Oxford, 1967.
[3] R.G. Horn, D.T. Smith, A. Grabbe, Contact electrification induced by monolayer modification of a surface and relation to acid-base interactions, Nature 366 (1993) 442–443.
[4] J. Lowell, A.C. Rose-Innes, Contact electrification, Adv. Phys. 29 (1980) 947–1203.
[5] C. Liu, A.J. Bard, Electrostatic electrochemistry at insulators, Nat. Mater. 7 (2008) 505–508.
[6] A. Li, Y. Zi, H. Guo, Z.L. Wang, F.M. Fernandez, Triboelectric nanogenerators for sensitive nano-coulomb molecular mass spectrometry, Nat. Nanotechnol. 12 (2017) 481–487.
[7] C. Yao, X. Yin, Y. Yu, Z. Cai, X. Wang, Chemically functionalized natural cellulose materials for effective triboelectric nanogenerator development, Adv. Funct. Mater. 27 (2017) 1700794.
[8] J.W. Lee, H.J. Cho, J. Chun, K.N. Kim, S. Kim, C.W. Ahn, I.W. Kim, J.Y. Kim, S.W. Kim, C. Yang, J.M. Baik, Robust nanogenerators based on graft copolymers via control of dielectrics for remarkable output power enhancement, Sci. Adv. 3 (2017) e1602902.
[9] S. Niu, Z.L. Wang, Theoretical systems of triboelectric nanogenerators, Nano Energy 14 (2015) 161–192.
[10] J. Shao, T. Jiang, W. Tang, X. Chen, L. Xu, Z.L. Wang, Structural figure-of-merits of triboelectric nanogenerators at powering loads, Nano Energy 51 (2018) 688–697.
[11] J.L. Heilbron, Electricity in the 17th and 18th Centuries: A Study of Early Modern Physics, UC Press, 1979.
[12] A.F. Diaz, R.M. Felix-Navarro, A semi-quantitative tribo-electric series for polymeric materials: the influence of chemical structure and properties, J. Electrost. 62 (2004) 277–290.
[13] F. Galembeck, T.A.L. Burgo, L.B.S. Balestrin, R.F. Gouveia, C.A. Silva, A. Galembeck, Friction, tribochemistry and triboelectricity: recent progress and perspectives, RSC Adv. 4 (2014) 64280–64298.
[14] L.S. McCarty, G.M. Whitesides, Electrostatic charging due to separation of ions at interfaces: contact electrification of ionic electrets, Angew. Chem. Int. Ed. 47 (2008) 2188–2207.
[15] H.T. Baytekin, A.Z. Patashinski, M. Branicki, B. Baytekin, S. Soh, B.A. Grzybowski, The mosaic of surface charge in contact electrification, Science 333 (2011) 308–312.
[16] C. Xu, Y. Zi, A.C. Wang, H. Zou, Y. Dai, X. He, P. Wang, Y.C. Wang, P. Feng, D. Li, Z.L. Wang, On the electron transfer mechanism in the contact electrification effect, Adv Mater 30 (2018) 1706790.
[17] J. Peng, S.D. Kang, G.J. Snyder, Optimization principles and the figure of merit for triboelectric generators, Sci. Adv. 3 (2017) eaap8576.
[18] R.D.I.G. Dharmasena, K.D.G.I. Jayawardena, C.A. Mills, R.A. Dorey, S.R.P. Silva, A unified theoretical model for triboelectric nanogenerators, Nano Energy 48 (2018) 391–400.
[19] R.D.I.G. Dharmasena, K.D.G.I. Jayawardena, C.A. Mills, J.H.B. Deane, J.V. Anguita, R.A. Dorey, S.R.P. Silva, Triboelectric nanogenerators: providing a fundamental framework, Energ. Environ. Sci. 10 (2017) 1801–1811.
[20] M. Siek, W. Adamkiewicz, Y.I. Sobolev, B.A. Grzybowski, The influence of distant substrates on the outcome of contact electrification, Angew. Chem. Int. Ed. 57 (2018) 15379–15383.

[21] S.M. Niu, Y. Liu, S.H. Wang, L. Lin, Y.S. Zhou, Y.F. Hu, Z.L. Wang, Theoretical investigation and structural optimization of single-electrode triboelectric nanogenerators, Adv. Funct. Mater. 24 (2014) 3332–3340.
[22] Y. Zi, C. Wu, W. Ding, Z.L. Wang, Maximized effective energy output of contact- separationtriggered triboelectric nanogenerators as limited by air breakdown, Adv. Funct. Mater. 27 (2017) 1700049.
[23] J. Shao, M. Willatzen, T. Jiang, W. Tang, X. Chen, J. Wang, Z.L. Wang, Quantifying the Power Output and Structural Figure-Of-Merits of Triboelectric Nanogenerators in a Charging System Starting from the Maxwell's Displacement Current, https://doi.org/10.1016/j.nanoen.2019.02.051.
[24] Z.L. Wang, On Maxwell's displacement current for energy and sensors: the origin of nanogen- erators, Mater. Today 20 (2017) 74–82.
[25] Y. Zi, S. Niu, J. Wang, Z. Wen, W. Tang, Z.L. Wang, Standards and figure-of-merits for quantifying the performance of triboelectric nanogenerators, Nat. Commun. 6 (2015) 8376.
[26] S.M. Niu, S.H. Wang, L. Lin, Y. Liu, Y.S. Zhou, Y.F. Hu, Z.L. Wang, Theoretical study of contact-mode triboelectric nanogenerators as an effective power source, Energ. Environ. Sci. 6 (2013) 3576.